A Hybrid Computational and Analytical Model of Irrigation Drip Emitters

by

Jaya Narain

S.B., Massachusetts Institute of Technology (2015)

Submitted to the Department of Mechanical Engineering
in partial fulfillment of the requirements for the degree of

Master of Science in Mechanical Engineering

at the

MASSACHUSETTS INSTITUTE OF TECHNOLOGY

June 2017

Author ..... Signature redacted
Department of Mechanical Engineering
May 12, 2017

Certified by ..... Signature redacted
Amos G. Winter, V.
Assistant Professor of Mechanical Engineering
Thesis Supervisor

Accepted by ..... Signature redacted
Rohan Abeyaratne
Chairman, Department Committee on Graduate Theses

A Hybrid Computational and Analytical Model of Irrigation Drip Emitters

by

Jaya Narain

Submitted to the Department of Mechanical Engineering
on May 12, 2017, in partial fulfillment of the
requirements for the degree of
Master of Science in Mechanical Engineering

Abstract

This thesis details a hybrid computational and analytical model to predict the performance of inline pressure-compensating (PC) drip emitters. A verified CFD model is used to predict flow behavior through tortuous paths. A method of extracting a pressure scaling parameter from the CFD results for use in an analytical model is presented. Analytical expressions that describe the bending of asymmetric rectangular membranes in inline drip emitters are detailed. These expressions are combined with finite element analysis (FEA) describing the shearing behavior of the membrane to model the total flow resistance through the emitter. Analytical expressions that describe the fluid mechanics of duct and turbulent flows are used to predict the net flow rate out of the emitter. The final model is verified for three distinct emitter geometries. The hybrid model presented in this paper has wide applicability – it can be applied to asymmetrical emitter geometries that have tortuous paths and other complex flow geometries. The hybrid model benefits from the accuracy of computational modeling for complex flows and contact interactions, and the processing speed of analytical models. Because of its accuracy and speed, the model can be used reliably as a design tool for inline PC emitters.

Thesis Supervisor: Amos G. Winter, V.
Title: Assistant Professor of Mechanical Engineering

Acknowledgments

I am grateful to many people and groups for their support during this project. I would like to warmly thank:

- Guillermo, for his endless support, motivation and advice. I am lucky to have shared this adventure with you, and I look forward to many more together.
- My parents, for supporting my pursuits and goals through the years
- Amos, for his guidance and feedback on my work, and for his enthusiasm and encouragement throughout the research process
- Jain Irrigation, and particularly Abhijit Joshi and Sachin Patil, for providing insight, knowledge, and advice on irrigation technology and for their financial support of this project
- My undergraduate research assistants, Trang Luu and Andrea Meister, for their dedication and help with data collection
- My lab mates in the Global Engineering and Research Lab for their friendship and willingness to lend a hand when needed
- My friends for their support and camaraderie throughout this adventure
- The Tata Center of Design and Technology for its advice and community
- The National Science Foundation Graduate Research Fellowship Program, for their financial support of my research

Contents

List of Figures

List of Tables

Chapter 1

Introduction

1.1 Summary of contributions

This thesis develops a hybrid analytical-computational model that describes the behavior of pressure-compensating (PC) inline drip emitters. The work:

- details a comprehensive model for drip emitters that has wide applicability – it can be applied to emitters with tortuous paths or other complex flow geometries, and can be applied to emitters with asymmetrical pressure-compensating chambers
- presents new methods for condensing information from computational fluid dynamics (CFD) and finite element analyses of drip emitters into parameters and functions that can be easily combined with analytical equations
- validates the model using three commercial products with very high fidelity over a range of geometries and flow rates. The model predictions were reliably within the 95 percent confidence interval of experimental data.
- significantly reduces processing requirements compared to a high-accuracy, purely computational model

The hybrid model benefits from the accuracy of computational modeling and the

processing time of analytical modeling. It has higher fidelity than a fully analytical model and is less computationally intensive than a fully finite element model.

Using five 2.4 GHz Intel Xeon Processor cores in parallel, the hybrid computational-analytical model presented herein can generate predictions of emitter behavior in 30 minutes. The hybrid model's predictions are comparable in accuracy and resolution to a solely computational model, which would require more than six hours using the same processor.

The underlying theory illuminates the principles of fluid and structural mechanics that tie the performance of a drip emitter to its geometry. The resulting high fidelity, computationally-light model is a useful design tool that can be used to improve the design of drip irrigation emitters.

1.2 Outline of content

The introduction provides background on irrigation technology and describes the motivation and potential impact of the research.

Chapter two describes prior art on emitter design, and reviews literature on modeling the behavior of drip emitters.

Chapter three details a computational fluid dynamics (CFD) model for flow through tortuous paths, validates the CFD model, and details a methodology for condensing the information provided by CFD into a form that can be used in the hybrid model.

Chapter four describes methods used to model the pressure-compensating mechanism in the emitter: the bending of a rectangular membrane in a drip emitter using analytical methods, the deformation of a section of the membrane into a small channel using finite element analysis (FEA), and the flow beneath the membrane.

Chapter five characterizes the overall fidelity of the hybrid analytical-computational model and discusses possible sources of error.

1.3 Drip irrigation: technology overview

The use of irrigation in agriculture dates to Mesopotamia in 6000 BC [1]. Irrigation technology has been developed over thousands of years to suit various geographical needs. Today, there are four major types of irrigation technologies: (1) surface, (2) subsurface, (3), sprinkler, and (4) micro irrigation, or drip irrigation [2]. Drip irrigation is a method of irrigation that delivers a steady, controlled flow of water directly to a plant's roots. A drip irrigation system typically consists of a network of pipes connected to a pump, and a water and energy source (Figure 1-1).

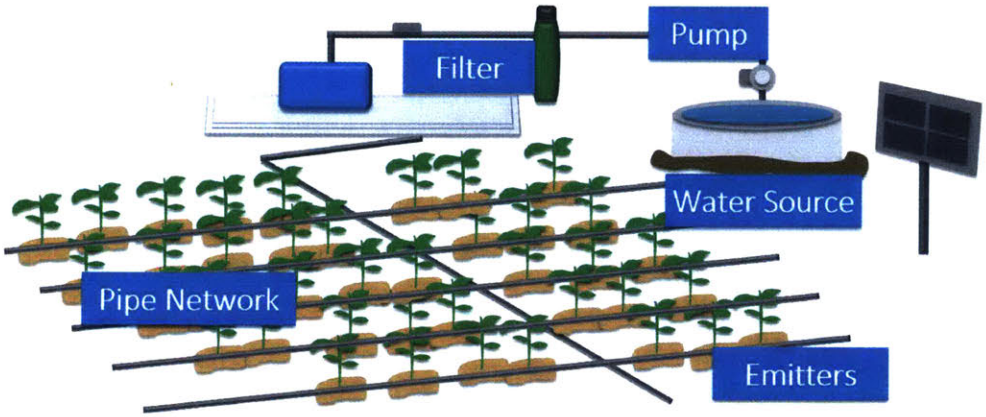

Figure 1-1: **Layout of drip irrigation system**

Drip irrigation delivers water via emitters embedded in a network of pipes. Emitters control the flow rate of water delivered to crops. This paper focuses on inline emitters, which are embedded inside pipes and sold as part of tubing. Online emitters are packaged and sold separately from piping and must be installed by the farmer. Because they do not require installation, inline emitters are generally more popular than online emitter types and account for a significant majority of drip emitter sales [3].

Emitters can be described as pressure compensating (PC) or non-pressure compensating (NPC). PC drip emitters (Figure 1-2) deliver a constant flow rate over a wide range of pressures. The activation pressure is defined as the pressure at which the flow-compensating behavior begins (Figure 1-3). .

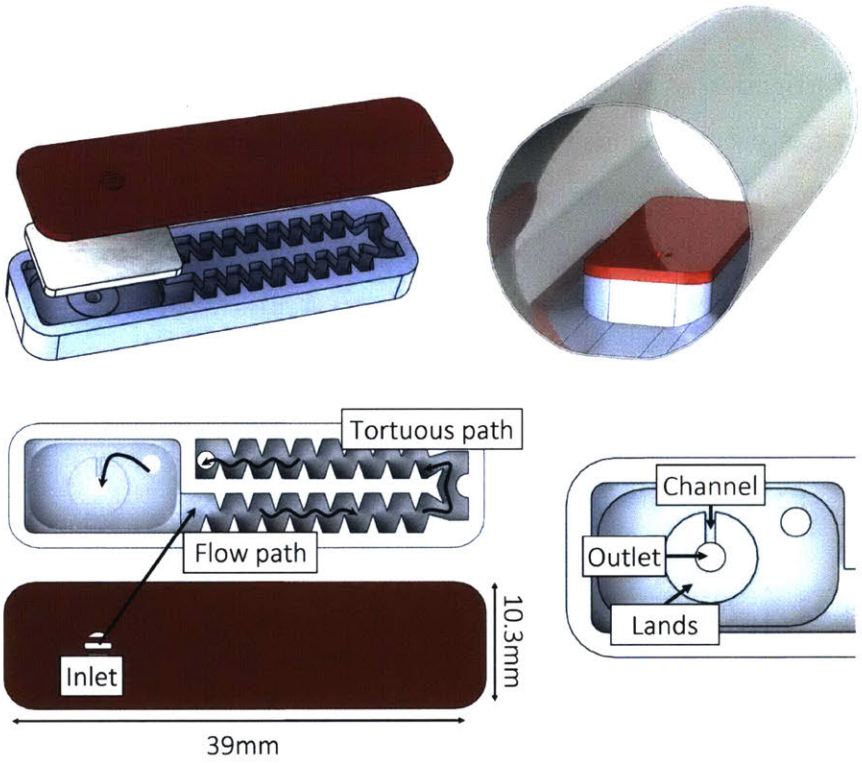

Figure 1-2: **PC Inline Emitter: Jain Irrigation Turbo Cascade 2 L/hr emitter.** Inline drippers are embedded in pipes during the manufacturing process. Water from the inlet flows to the start of the tortuous path, through the tortuous path, and into a rectangular chamber that has a small channel that provides passageway though circular lands. A silicone membrane rests inside the rectangular chamber, on top of the lands.

Individual emitters are characterized by their activation pressure (for PC emitters) and flow rate, and emitter performance is characterized by the variation in flow rate compared to the manufacturer's specification and the likelihood of clogging. PC drip emitters typically consist of a tortuous flow path and a flexible membrane that deforms to control the flow resistance (Figure 1-2). The deformation of the membrane depends on the input pressure P_1, the pressure underneath the membrane P_2, and atmospheric pressure P_a. (Figure 1-4). In PC drippers, the design of the tortuous path affects the activation pressure of the emitter and the flow rating of the emitter. NPC drip emitters typically consist solely of a tortuous flow path (Figure 1-5). In

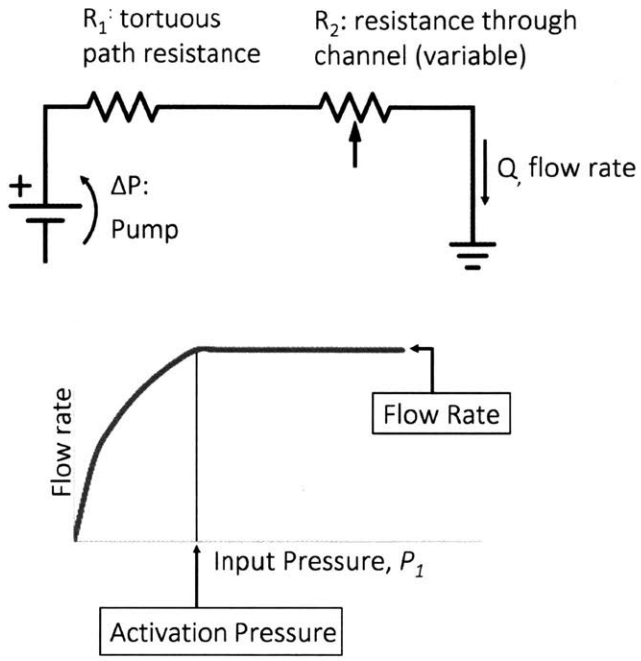

Figure 1-3: **Pressure-compensating behavior of emitters.** The flow rate through the emitter is a function of the flow resistance through the emitter. As P_1 increases, the resistance through the channel R_2 also increases, resulting in a proportionally lower flow rate. This pressure-compensating mechanism leads to a constant flow rate at pressures higher than the activation pressure of the emitter.

NPC drip emitters, the design of the tortuous path dictates the flow rate behavior as a function of pressure for the device [4].

1.4 Research motivation

Drip irrigation is advantageous because it reduces water consumption and can increase crop yield compared to conventional methods. A study conducted in India showed water savings between 20-40 percent and increases in yield between 20-50 percent with drip irrigation compared to furrow irrigation, depending on the crop grown [5]. Drip irrigation can enable farmers to grow crops under conditions where they could not otherwise do so (e.g. with strict water constraints or in dry seasons), allow farmers to grow a wider array of crops, and save on labor and fertilizer costs [6]. Because drip

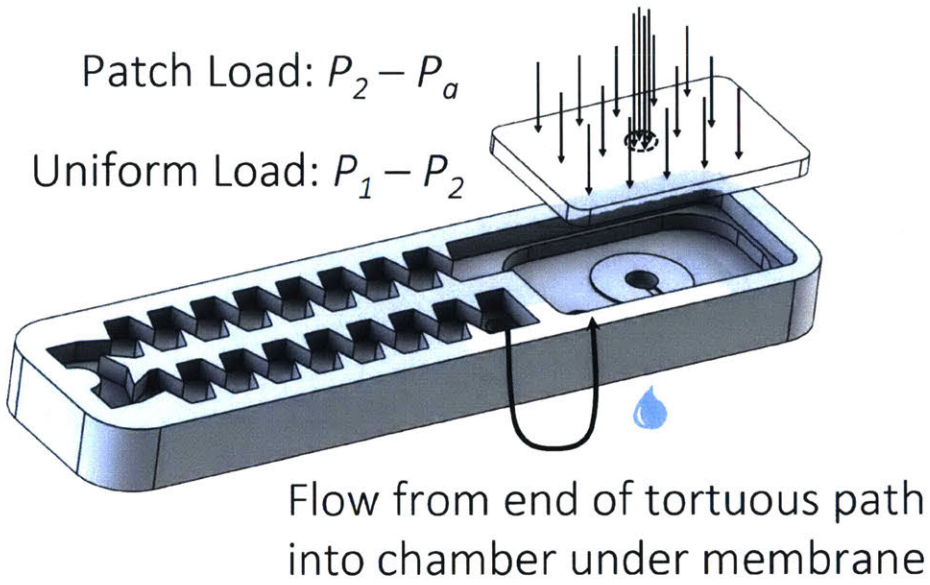

Figure 1-4: **Overview of PC mechanism**. After the flow leaves the tortuous path, it enters a chamber underneath the membrane. The pressure differential across the membrane is modeled as a uniform load over the entire area of the membrane and a patch load over the portion of the membrane above the outlet.

irrigation delivers water and nutrients precisely, it can also help farmers transition to higher-value crops that require careful cultivation methods. Drip irrigation has several other benefits, like reduced sensitivity to variations in salinity and water quality due to lower water volumes and increased protection from diseases and pests by isolating soil wetness to the plant's root zone [7].

Despite its benefits, drip irrigation has very low adoption rates (Figure 1-6), particularly in developing nations. In India, a developing nation with a large agricultural sector, less than one percent of land is cultivated using drip irrigation [2]. The high cost of drip irrigation systems is one of several major barriers to adoption. Drip irrigation systems require significant pumping power to operate. The power required depends on the minimum pressure required by the system and the flow rate through the system, by

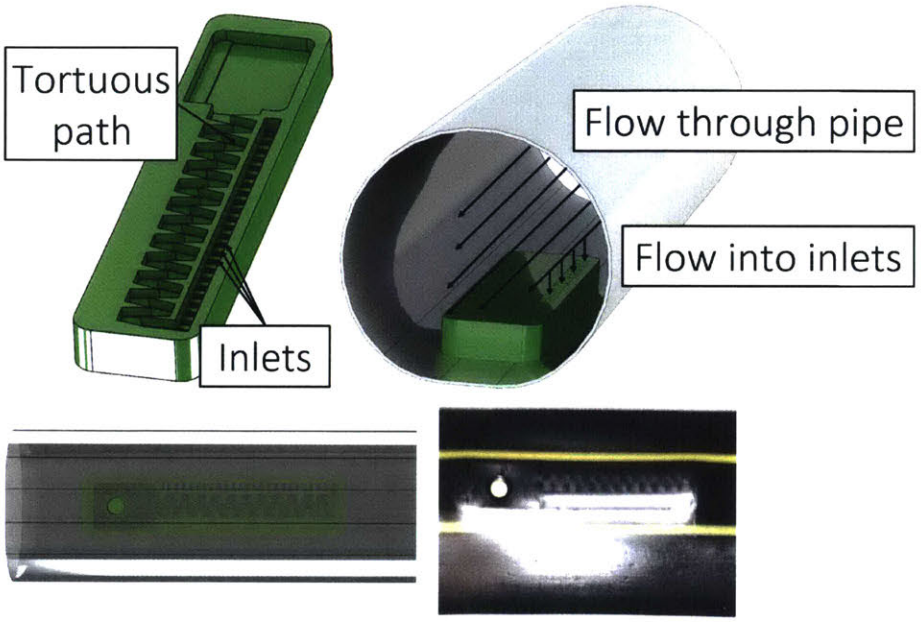

Figure 1-5: **NPC Inline Emitter: Turbo Excel 1.6 L/hr** NPC emitters consist of an array of inlets leading to a tortuous path. The pipe wall contains the flow within the tortuous path. The emitters are embedded in pipes during a heat-forming process which results in portions of the tube being pushed into the tortuous path.

$$W = P \times Q, \tag{1.1}$$

where W is the power, P is the operating pressure, and Q is the flow rate. Reducing the pressure required to operate a drip irrigation system can significantly reduce the power required by the the overall system, and lower costs for off-grid farmers by enabling them to use smaller pumps, fewer panels in solar applications, and less diesel in diesel pumps. There is a need for high-performance, low-power, low-cost drip irrigation systems. The longer term goal of this research is to use the design tool developed in this thesis to design PC inline drip emitters with an activation pressure of approximately 0.10 bar, for use in energy efficient drip systems.

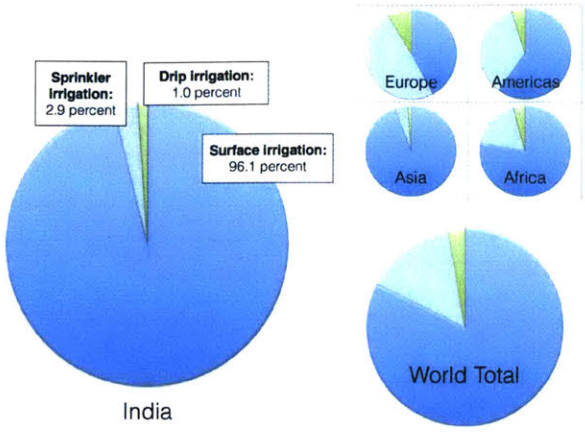

Figure 1-6: **Global adoption rates of drip and sprinkler irrigation**, data from [2]

1.4.1 Potential impact in India

In India, where electricity is heavily subsidized, energy costs are a particularly large burden for off-grid farmers, who must use costly diesel or solar systems [8]. A drip irrigation system using emitters of activation pressure of 0.10 bar is estimated to cost approximately 30 percent less than (Figure 1-7) an irrigation system using emitters with activation pressure 1 bar [9].

In India, using energy efficient drip systems may have the greatest impact on system cost in regions with surface water sources and poor electrification. The reduction in energy consumption has the highest impact for farmers who have a surface water source (Table 1.1). For farmers with groundwater sources, the driving power requirement is the power required to pump water from depth to the surface; improving the energy efficiency of the drip system will have a proportionally smaller impact on their overall energy usage.

Northeast India – particularly Bihar – has particularly low usage of electric pumps and groundwater sources (Figure 1-8). Neighboring states Jharkhand and Uttar Pradesh have relatively large reserves of very shallow groundwater sources [10]. Low activation pressure drip systems may have a markedly high impact on the cost of drip irrigation in these regions.

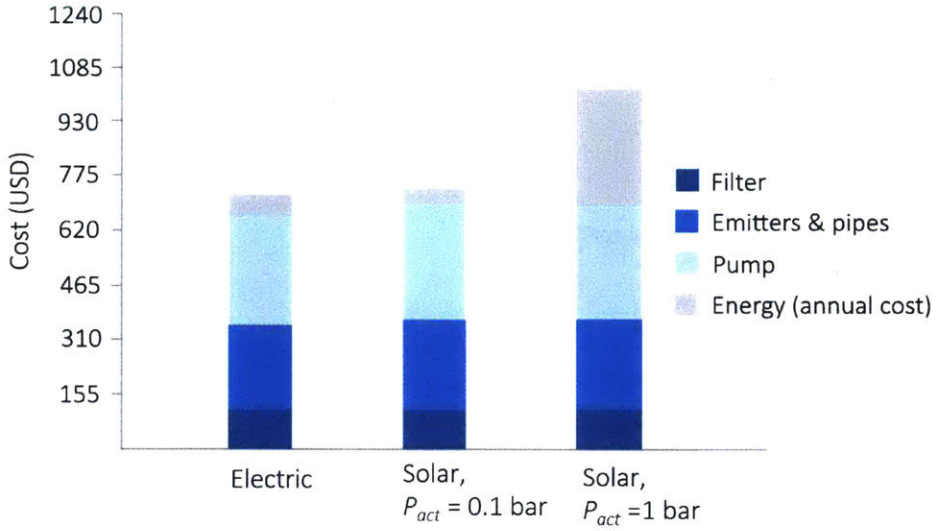

Figure 1-7: **Estimated costs for a drip irrigation system**, data from the model described in [9]

The income of small and mid-size farmers on-grid in India is directly affected by the poor reliability and limited supply of power for irrigation [8]. Table 1.1 provides the energy consumption/acre for drip irrigation systems that use emitters of activation pressure 1 bar and 0.1 bar. In many regions in India, the average power available per farm is not sufficient to run a drip irrigation system that has emitters activated at 1 bar, especially for farmers with groundwater sources. Drip systems with emitters activated at low pressure could be used reliably in many more areas.

Table 1.1: **Energy consumption of drip irrigation system (kW/acre)**, data from model described in [9]

Depth of water source (m)	Activation pressure: 0.1 bar	Activation pressure: 1 bar
0	0.055	0.418
15	0.218	0.581
30	0.382	0.745
50	0.6	0.962

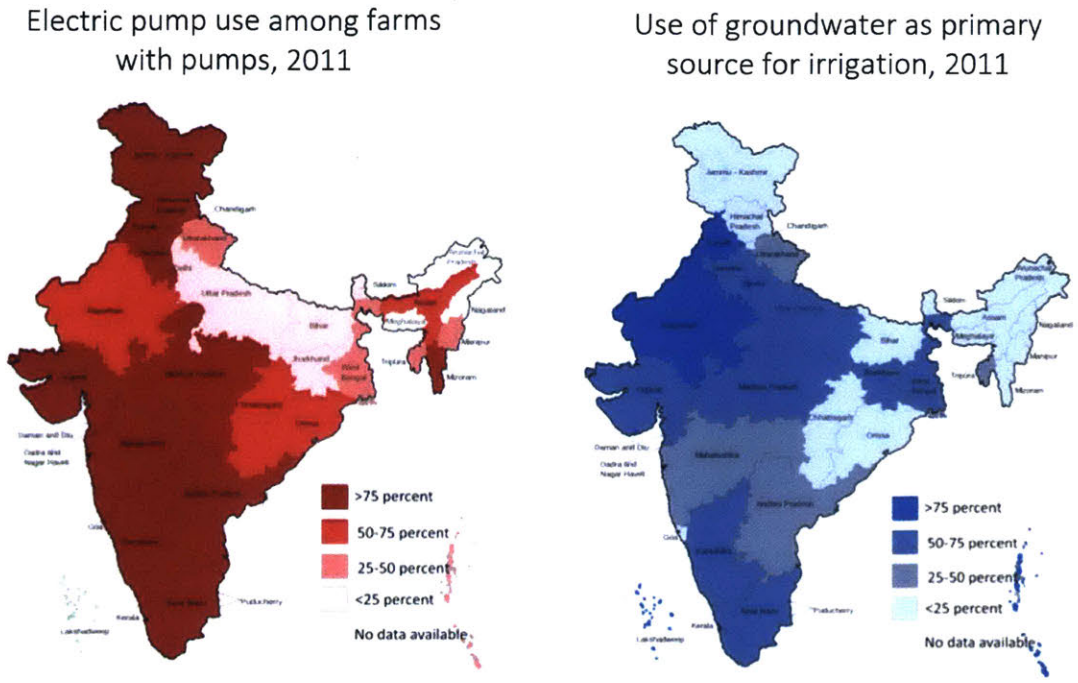

Figure 1-8: **Energy and water sources**, data from [11]

1.4.2 Potential global impact

In the Middle East, municipal water facilities commonly supply limited pressure water to farmers [13]. Low power drip systems could enable more use of drip systems among farmers with restricted energy access or water pressure constraints.

Globally, water and energy are becoming increasingly scarce resources. Water-saving technologies like drip irrigation are becoming more of a necessity.

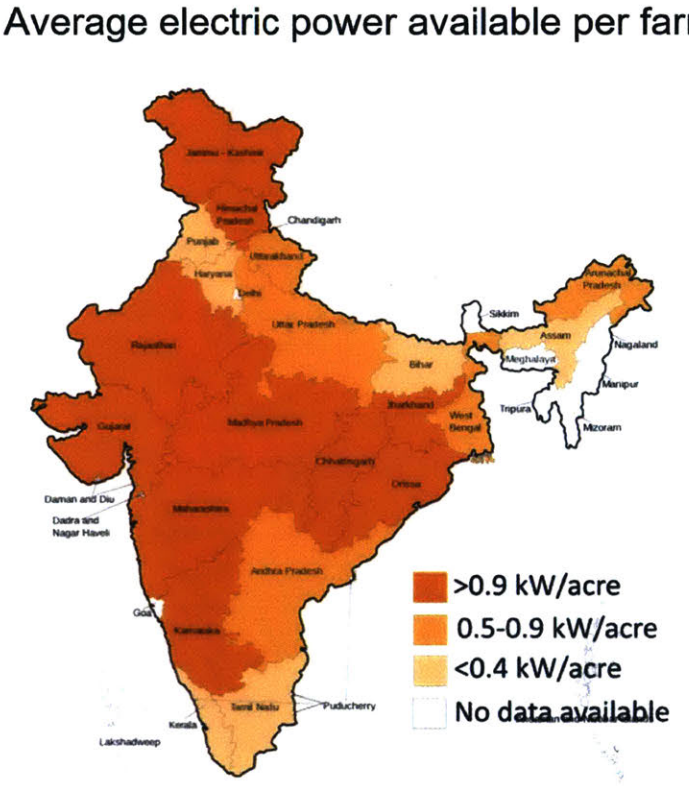

Figure 1-9: **Average electric power available per farm**, data from [12]

Chapter 2

Prior Art

Drip irrigation began over 2000 years ago, with the use of buried clay pots in China. The pots were filled with water before burial, and the water slowly seeped through the clay pores. The seepage rate depends on the uptake rate of water from the soil by plants [14]. Farmers in Afghanistan began to use clay pipes for irrigation and seepage in the 1800s [15]. The first modern plastic drip emitters were developed in Israel by Simcha and Yeshayahu Blass. Their work eventually became the basis for the Israeli company Netafim [16]. Other major global suppliers of drip irrigation equipment include Jain Irrigation Ltd, Rain Bird, and Toro.

2.1 Overview of available products

There is a wide variety of existing emitter products. Major manufacturers mass produce plastic drip emitters with a variety of flow rates and designs. Non-profits and grassroots organization have made efforts to design and distribute low-cost alternatives.

2.1.1 Products made my major manufacturers

Figure 2-1 summarizes a selection of commercially available PC inline drippers made by major drip manufacturers. Netafim is the largest global distributor of drip prod-

ucts, followed by Jain Irrigation [17]. The following abbreviations are used in the table: "AD" for anti-drainage, "AL" for anti-leakage, "AS" for anti-siphoning, "SF" for self-flushing, and "SC" for self-cleaning.

Figure 2-2 summarizes the number and type of a sampling inline PC emitters available over a range of activation pressures. Only five of the emitters surveyed had activation pressures lower than 0.4 bar. The activation pressure of emitters with higher flow rates tended to be higher. The median activation pressure was 0.5 bar. The information shows a gap in the available product space for emitters that have a low activation pressures for a range of flow rates.

2.1.2 Non-profit and grassroots products

Several non-profits and major companies have designed low-cost drip kits specifically for smallholder farmers, called affordable micro irrigation technologies (AMITs). These systems are generally gravity driven, and use perforated piping, extended tubes, or bucket and drum kits in place of plastic emitters [18].

Drip kits produced by the International Development Enterprises (IDE) use piping with punched holes and micro tubes to control water flow. The kits have been shown to have yield increases of up to 30 percent, and reduce water consumption per area by 30-70 percent compared to furrow irrigation. The IDE drip kits can be used effectively on plots under 0.4 hectares [19]. A study on the marketing effectiveness of IDE India bucket kits found that even though the cost of the system was lower than conventional commercial products (Figure 2-1), generally smallholder farmers still did not purchase the kits without subsidies. The farmers surveyed understood that the IDE drip kits has limitations compared to other commercial products with respect to long-term use and expansion potential, and were hesitant to invest in the AMIT products [20]

Farmers who saw the utility in micro-irrigation but wanted more affordable implementations have developed several innovative drip irrigation tools. Farmers in the Madhya Pradesh and Maharashtra areas began experimenting with bicycle rubber tubes as drip tubes. After initial experiments were unsuccessful, continued innova-

tion eventually led to a system called Pepsee, which utilizes plastic rolls traditionally used to make ice candy in a drip system [21].

The use of Pepsee systems has spread due to a need among farmers with stressed water resources for an affordable, more efficient irrigation technique. For one acre of cotton, a Pepsee system costs only 93 USD. The cost of the Pepsee and micro-tube systems is entirely market driven, unlike the commercial systems which are affected by subsidy structures. Pepsee systems have several limitations, including: they must be replaced yearly, the straws are prone to clogging, uneven water distribution, and wind blow away the tubes [21].

In Meghalaya, farmers have historically used bamboo shoots in drip irrigation systems [22]. Some farmers also micro-irrigate using plastic tubes without emitters, by punching varying numbers of holes in tubing to achieve more uniform flow (e.g., one hole at the beginning of a lateral and three holes at the end of a lateral) or by attaching micro-tubes of varying lengths to the larger tubes.

2.2 Literature review on emitter modeling

Improving the performance of drip emitters could encourage greater adoption of the technology and is a topic of interest in both research and industry. Understanding the flow behavior through tortuous paths is a key component to designing improved emitter technologies. Palau-Salvador et. al. suggested computational fluid dynamics (CFD) analysis of tortuous paths as a powerful tool for emitter design [23]. Previous studies on tortuous path behavior have used CFD as a tool to analyze the effects of altering dentate geometry in flow paths [24]. Wei, at. all used CFD to characterize the effect of rectangular, trapezoidal, and triangle labyrinth geometries [25].

Some full models of pressure-compensating emitter behavior exist in the literature. Shamshery et. al. [26] approximated the flow behavior of circular PC online emitters that do not have tortuous paths by using analytical expressions for the deflection of the flexible membrane and corresponding flow restriction within the PC emitter. Zhengying [27] modeled cylindrical inline emitters with high accuracy using

computational fluid structure interactions (FSI) methods. Wang et. al. used FSI to model the behavior of circular online drip emitters with high accuracy [28].

The purely analytical model published by Shamshery et. al. has very low computational time, but has some error when applied over a range of flow rates [26]. CFD models, while accurate, can require significant user input to make robust changes to complex geometry structures. CFD models of emitters with labyrinth flow paths and fluid-structure interactions also require significant computational power and time.

Vendor	Product Name	Flow rates (L/hr)	Pressure-Compensating Range (bar)	Recommended Use	Notes
Jain	Turbo Cascade PC, PCAS, and PCNL	1, 1.5, 2, 3.6	0.49-3.92	PC & PCNL: Greenhouses, vegetables, orchards; PCAS: closely-spaced crops	Flat; AS or AL
Jain	Turbo Line	16mm OD: 1.6, 2, 2.6, 4; 20mm OD: 1.0, 1.6, 2.6, 4.3	0.49-3.93	Greenhouses, vegetables, orchards	Cylindrical
Jain	Turbo Top	1.1, 1.6	0.39-2.45	Greenhouses, vegetables, orchards	Flat
Rain Bird	A5 PC Dripline	1.2, 1.6, 2, 2.3, 4	0.48-4.1	Vineyards and orchards	Flat; SF
Netafim	UniRam RC and AS	0.7, 1, 1.6, 2.3, 3.5	0.5-4	Deciduous & tree irrigation; RC: on-surface row crops; AS: greenhouses, sub-surface row crops	Flat; SC, SF or AS
Netafim	UniRam CNL	0.7, 1, 1.6, 2.3, 3.6	1.0-4.0	Greenhouses, deciduous & tree irrigation, sub-surface row crops	Flat; SC, AS, AD
Netafim	UniRam HCNL	0.85, 1.25, 2, 2.9, 4.4	1.5-4	Greenhouses, deciduous & tree irrigation	Flat; SC, AS, AD
Netafim	DripNet PC	0.4, 0.6, 1, 1.6, 2, 3, 3.8	0.4 (0.25 - 2.5) 0.6 (0.25 -2.5) 1.0 (0.4-3) 1.5 (0.4-3) 2, 3 (0.4-3.5) 3.8 (0.6-3.5)	Row crops	Flat; SC
Netafim	DripNet PC AS thick-walled	0.6, , 1.6, 2, 3, 3.8	0.6 (0.25 -2.5) 1.0 (0.4-3) 1.5 (0.4-3) 2, 3 (0.4-3.5) 3.8 (0.6-3.5)	Sub-surface row crops	Flat; SC, AS
NetaFi m	UniWine	0.7,1,1.6,2.3,3.5	0.5-4	Sub- and on-surface row crops	Flat; SC, SF, AS,
Netafim	DripWine	0.6, 1, 1.6, 2, 3, 3.8	0.6 (0.25 -2.5) 1.0 (0.4-3) 1.6 (0.4-3) 2, 3 (0.4-3.5) 3.8 (0.6-3.5)	On-Surface row crops	Flat; SC, SF, AS
Toro	Drip In PC	1-4.1	1.9-3.8		Cylindrical
Toro	Blueline PC	0.69-4.14	1, 1.5, 2, 4.		Flat; AS

Figure 2-1: **Selected commercially available inline pressure-compensating drip emitters**

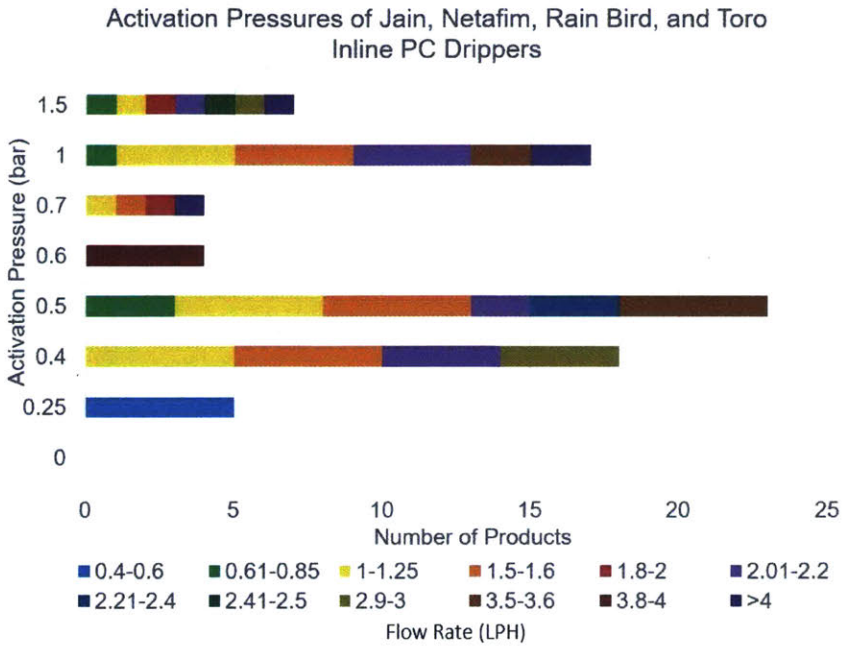

Figure 2-2: **Survey of activation pressure and flow rate of emitters from selected major manufacturers**. The following abbreviations are used: "AD" for anti-drainage, "AL" for anti-leakage, "AS" for anti-siphoning, "SF" for self-flushing, and "SC" for self-cleaning

Chapter 3

CFD Model of Tortuous Paths

The flow of water through the tortuous path in a drip emitter (Figure 1-2) has high- and low- velocity regions, recirculation zones, and strong wall effects. While these behaviors are difficult to model analytically, CFD can accurately describe the flow in a tortuous path. The information and insights obtained from CFD are used in the hybrid computational-analytical model of inline PC drip emitters presented in this thesis.

3.1 Model overview

Flow behavior of water through tortuous flow paths was modeled using the ANSYS CFX 16.0 package. NPC emitters (Figure 1-5), which consist only of an inlet system and tortuous flow path, were used to verify the capability of the CFD model to provide accurate results. The model geometry consisted of a single drip emitter, that had tortuous flow paths with dimensions equivalent to those of Jain Turbo Excel Plus 0.75, 1.6, and 4 L/hr emitters.

In NPC drippers, the tubing itself provides part of the wall that bounds the flow through the tortuous path. An inflation layer was used in the mesh at the interfaces between the fluid and emitter walls and between the fluid and piping to accurately model the flow near the walls. An inflation layer is a fine, controlled mesh near a wall that can capture the large gradients in flow properties characteristic of boundary

layers. The walls were modeled as smooth. A minimum element size on the faces of the fluid in contact with the dripper of $1.8 * 10^{-}4$ m was used to ensure a mesh sufficiently fine to capture the flow behavior. Test runs with smaller element sizes converged yielding the same results as runs with the cited element size. A shear stress transport model (SST) was used for turbulence, because flow separation and eddy formation in the flow path was expected.

A boundary condition of total pressure was set at the pipe inlet. Total pressure represents the pressure in the irrigation pipe before the flow enters the emitter, and was used as an independent variable. The inlet flow was defined as normal to the pipe inlet with medium turbulence. A boundary condition of average atmospheric static pressure was set at the dripper outlet.

The dimensions in the model were based on Turbo Excel Plus NPC inline emitters currently manufactured and distributed by Jain Irrigation. In the manufacturing facility of Jain Irrigation, a polyethylene tubing is heat-formed around a moving line of inline emitters. The heat-forming process results in portions of the tubing pushed into the tortuous path, altering the flow path dimensions. This obstruction was modeled as a $1.5 * 10^{-}4$ m reduction in the depth of the tortuous path based on the author's measurements of 0.75, 1.2, and 4 L/hr NPC Turbo Excel Plus dripline currently sold by Jain Irrigation.

Figure 3-1 shows a visualization of the flow through the emitter as computed by the model. This visualization is consistent with images published by Jain Irrigation [29] and Wei [25]. The bulk of the flow moves through the center of the flow path. Lower velocity recirculation zones are formed in the teeth of the labyrinth. Dependent on the flow velocity in the zone, recirculation zones may prevent sedimentation of particles that could clog the emitter, or may increase clogging potential [25].

3.2 Experimental set-up

To validate the model, experiments were conducted in the laboratory to characterize the performance of inline drip emitters. The inline emitter flow rates were measured

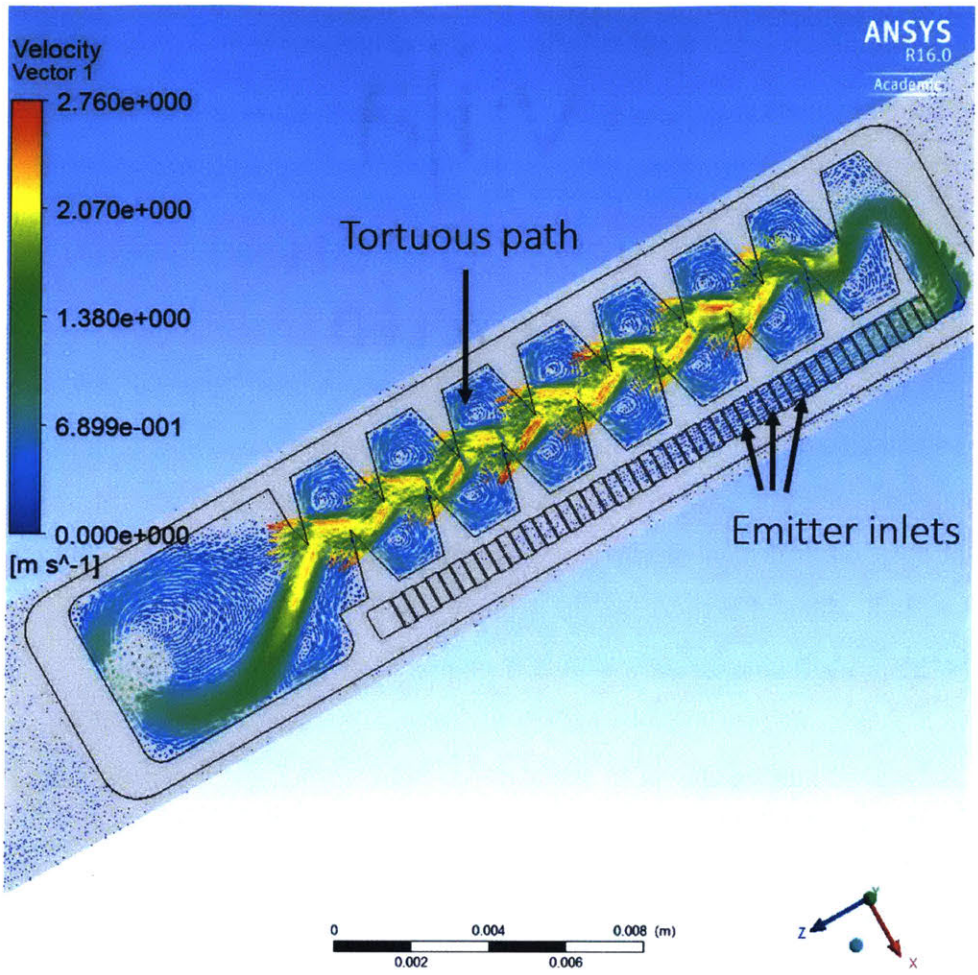

Figure 3-1: **Velocity of flow in a tortuous path**, computed using Ansys CFX. Flow enters the emitter through a row of rectangular inlets that lead directly to the tortuous path.

by flowing water of controlled pressure through 0.75 and 4 L/hr Jain Turbo Excel Plus driplines, measuring the pressure in the pipe near the inlet of the dripper using a pressure gauge, and measuring the flow rate out of the dripline using a graduated cylinder and timer (Figure 3-2). 1.6 L/hr drip emitters were not available for testing. Propagation of uncertainty was used to calculate the 95 percent confidence intervals for the experimental data.

3.3 CFD model fidelity

Figure 3-3 compares the results of the CFD model to experimental results and shows the geometry of each emitter. Figure 3-3 also reports the 95 percent confidence interval for the experimental measurements, which ranged from 0.23 to 0.40 L/hr for the 4 L/hr emitter, and from 0.06 to 0.15 L/hr for the 0.75 L/hr emitter. 1.6 L/hr emitters were not available for testing.

The coefficient of variation (cv) expresses the expected variation of flow rates among emitters of the same design due to manufacturing variations. The cv value for the tabulated data [29] for the 1.6 L/hr NPC emitter was estimated using experimental data published by the Irrigation Training and Research Center [30]. Based on these data, the cv for the 1.6 L/hr dripper was approximated as 8 percent.

The flow rate behavior as a function of pressure predicted by the CFD model (Figure 3-3) reliably overlapped with the 95 percent confidence interval of the experimental data, validating the CFD model predictions.

3.4 Scaling parameter based on path geometry

The primary objective of this thesis is to develop an accurate, computationally efficient model of PC emitters. Since PC emitters have other key design attributes in addition to a tortuous path (Figure 1-2), it is more difficult to experimentally verify the CFD model using PC emitters with existing hardware. The tortuous path is the only major flow control feature in NPC emitters. Since the CFD model is accurate for NPC emitters (Figure 3-3), it can also accurately predict flow behavior through the tortuous path in a PC emitter. PC emitters have similar architectures as NPC emitters. PC emitters generally have a membrane and pressure-compensating mechanism after a tortuous path, whereas NPC emitters have simply an outlet after a tortuous path (Figure 3-4).

Flow through PC and NPC emitters can be represented symbolically as electrical circuits (Figure 3-4). In an NPC emitter, the two major resistances are R_1, the

resistance through the inlet and tortuous path; and R_2, the resistance through the rectangular passage after the path and the outlet. In an PC emitter, the two major resistances are R_1, the resistance through the inlet and tortuous path; and R_2, the variable resistance through the pressure-compensating chamber after the path (Figure 1-2) and the outlet. In both PC and NPC emitters, $R_2 << R_1$. The circuit is analogous to a voltage divider, and the pressure P_2 in an NPC emitter is given by

$$P_2 = P_1(\frac{R_2}{R_1 + R_2}). \tag{3.1}$$

This expression can be rewritten to show that the ratio P_1/P_2 is a constant, denoted by K_{path}. That is,

$$\frac{P_1}{P_2} = \frac{1}{(\frac{R_2}{R_1+R_2})} = K_{path}, \tag{3.2}$$

or,

$$P_2 = \frac{P_1}{K_{path}}. \tag{3.3}$$

This expression describes the affect of the tortuous path on the flow independently of the flow rate of fluid through the path, a parameter that is difficult to compute or measure. This expression is a reasonable simplification when R_2 is a variable resistance - as in a PC emitter - for R_1 significantly larger than R_2. Over the range of pressures of interest for drip emitters, the resistance through the tortuous path, R_1, is the dominating resistance in both PC and NPC emitters. As such, this expression can be used to reasonably approximate K_{path} in PC emitters. The overall fidelity of the model and a discussion of its assumptions and limitations is presented in a later section. Equation 3.3 can be used to condense the simulation results into a single parameter that can be used in the hybrid model of PC emitter behavior.

The verified CFD model described in Section 3.1 was used to analyze the flow through tortuous paths of the Jain PC Turbo Cascade 1.1 L/hr, 2 L/hr and 3.8 L/hr emitters. A virtual sensor was placed at the end of the tortuous path to measure the pressure of the fluid at the end of the path, immediately before entering the chamber under the membrane. The simulation was run for sixteen distinct values of P_1, ranging from 0.1 to 1.6 bar, for each emitter geometry. The calculated scaling parameters with standard deviation for each emitter geometry are summarized in Table 3.1.

Table 3.1: **Summary of average scaling factors,** K_{path}, standard deviations calculated using CFD simulation results for sixteen input pressures for each PC inline emitter path geometry

Emitter flow rate (L/hr)	Average scaling factor	Standard Deviation
3.8	2.330	0.00040
2	2.772	0.0039
1.1	2.772	0.0011

The standard deviations on the scaling parameters were exceptionally small, signifying that the calculated value of the scaling factor is precise. The scaling factor for the 3.8 L/hr was the lowest. This means that the pressure drop in the tortuous path in the 3.8 L/hr emitter is less than the pressure drop in the paths for the 2 and 1.1 L/hr emitters. This result was expected because the path in the 3.8 L/hr emitter is wider and has fewer turns than the paths in other emitters (Figure 3-5). Despite differences in path geometry, the scaling factor for the 2 and 1.1 L/hr emitters were identical. It is hypothesized that this similarity is due to differences in recirculation between the two emitters (Figure 3-5). The 2 L/hr emitter has a wider flow path and fewer turns than the 1.1 L/hr emitter. However, the 1.1 L/hr emitter has significantly less recirculating flow than the 2 L/hr emitter. The relatively small proportion of recirculating flow in the 1.1 L/hr emitter may contribute to a smaller scaling factor for the emitter than would otherwise be expected in a tortuous path.

Because the standard deviation between measurements is so small, the scaling factor can be reliable determined by simulating the flow at only one input pressure.

Traditionally, the flow behavior through a tortuous path is characterized by fitting complex polynomial or exponential functions to a curve of flow rate as a function of pressure [27], [31]. Generating a full curve requires significantly more computational time than simulating the flow at only a single point. Simulating flow at only one input pressure took approximately ten minutes; simulating flow at multiple pressure to generate curves, as in Figure 3-3, took approximately four to six hours, dependent on the geometry of the path.

The method described in this thesis to encapsulate results from CFD describing flow behavior through tortuous paths requires simulation at only one input pressure. This significantly reduces the computational requirements to characterize flow through tortuous paths, as compared to typical methods which need information from a range of pressures to generate a curve [27], [31].

3.5 Sensitivity analysis of K_{path} on geometry

The parameter K_{path} is a function of the geometry of the tortuous path. A sensitivity analysis was conducted to better understand how the design of the path affects the scaling parameter. Six independent variables were identified that fully determine the geometry of the path (Figure 3-6): t, the triangle base width; y, the overlap between teeth; h, the triangle height; D, the trapezoid width, x, the depth of the path, and N, the number of turns

The base value for each variable was defined as its dimension in the 2 L/hr Turbo Cascade. The value of one variable was changed, while the values of all other variables were kept at their base values. The actual dimensions of the Turbo Cascade emitter are proprietary, and are labeled as 'base' in the tables and charts below. The alterations are defined by their deviation from the base value.

The results of the sensitivity analysis are summarized in Table 3.2 and Figure 3-7. The value of K_{path} decreases as the width of the triangle decreases. As the size of the triangle decreases, the magnitude to which it obstructs the flow path decrease.

Decreasing the height of the triangle - while maintaining all other variables at

constant values - resulted in an increase in K_{path}. This is likely because since y remained constant, the overall width of the flow path decreased, resulting in larger flow resistance. Increasing the height of the triangle also cause K_{path} to increase. This is likely because the longer triangle had a greater intrusion into the flow path, resulting in larger flow resistance. Greater resolution in the sensitivity analysis is needed to better understand this design trade-off.

In the base design, there is positive gap y between the tips of the teeth. At the design point $y - 0.25$, there is no gap and no overlap between the tips of the teeth. At the design point $y - 0.5$, the tips of the teeth overlap. Having either a positive gap or overlap between the tips of the teeth correlates to a higher value of K_{path}.

Within the range of values tested, K_{path} had relatively low sensitivity to D and x. K_{path} was most sensitive to N. As N decreased, the flow path shorter and less tortuous, and K_{path} also decreased.

Table 3.2: **Sensitivity of K_{path} on tortuous path geometry**

N	D	t	y	h	x	K_{path}
Base	Base	Base	Base	Base	Base	2.77
-6	Base	Base	Base	Base	Base	2.41
-12	Base	Base	Base	Base	Base	2.19
Base	-0.1	Base	Base	Base	Base	2.76
Base	-0.2	Base	Base	Base	Base	2.77
Base	Base	-0.2	Base	Base	Base	2.76
Base	Base	-0.5	Base	Base	Base	2.46
Base	Base	Base	-0.25	Base	Base	2.53
Base	Base	Base	-0.5	Base	Base	2.85
Base	Base	Base	Base	-0.5	Base	2.67
Base	Base	Base	Base	$+0.25$	Base	2.79
Base	Base	Base	Base	Base	-0.15	2.55
Base	Base	Base	Base	Base	$+0.15$	2.71

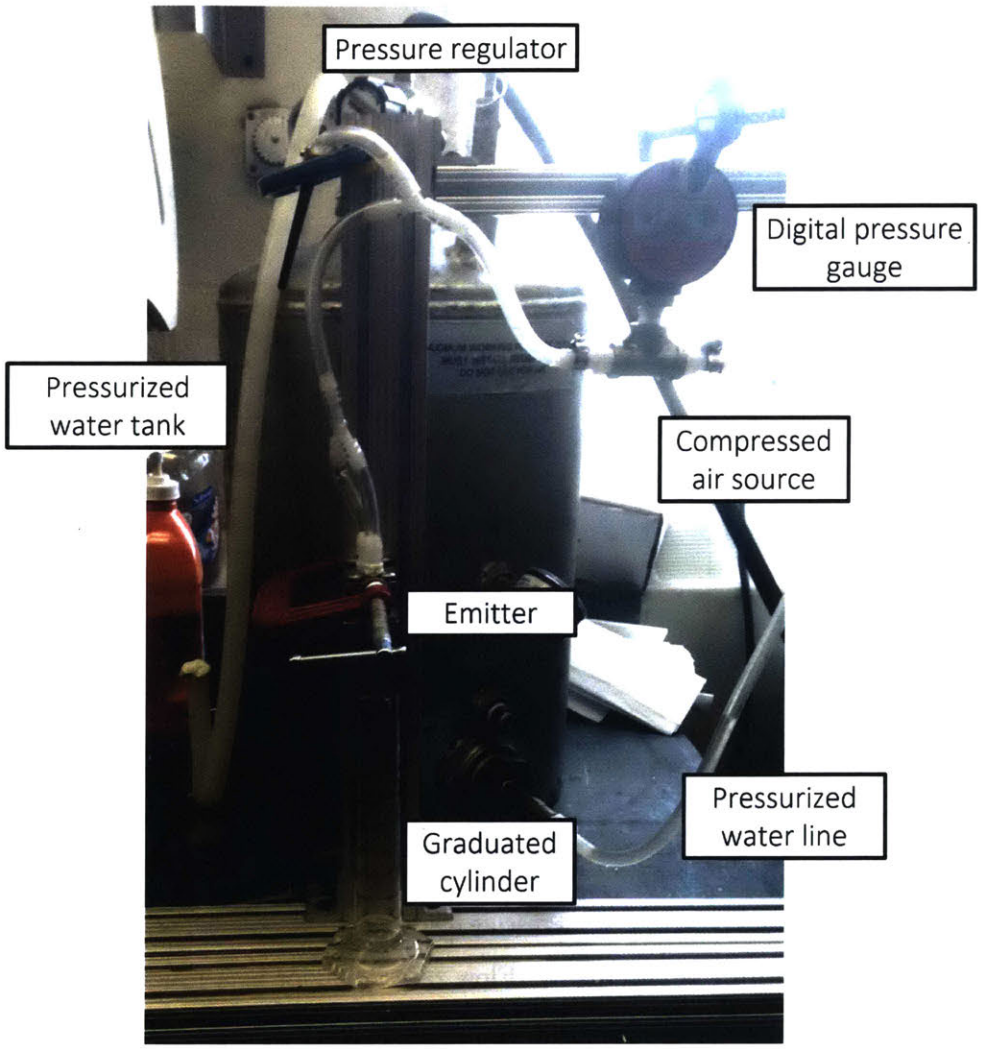

Figure 3-2: **Experimental set-up for testing the flow rate as a function of pressure for drip emitters**

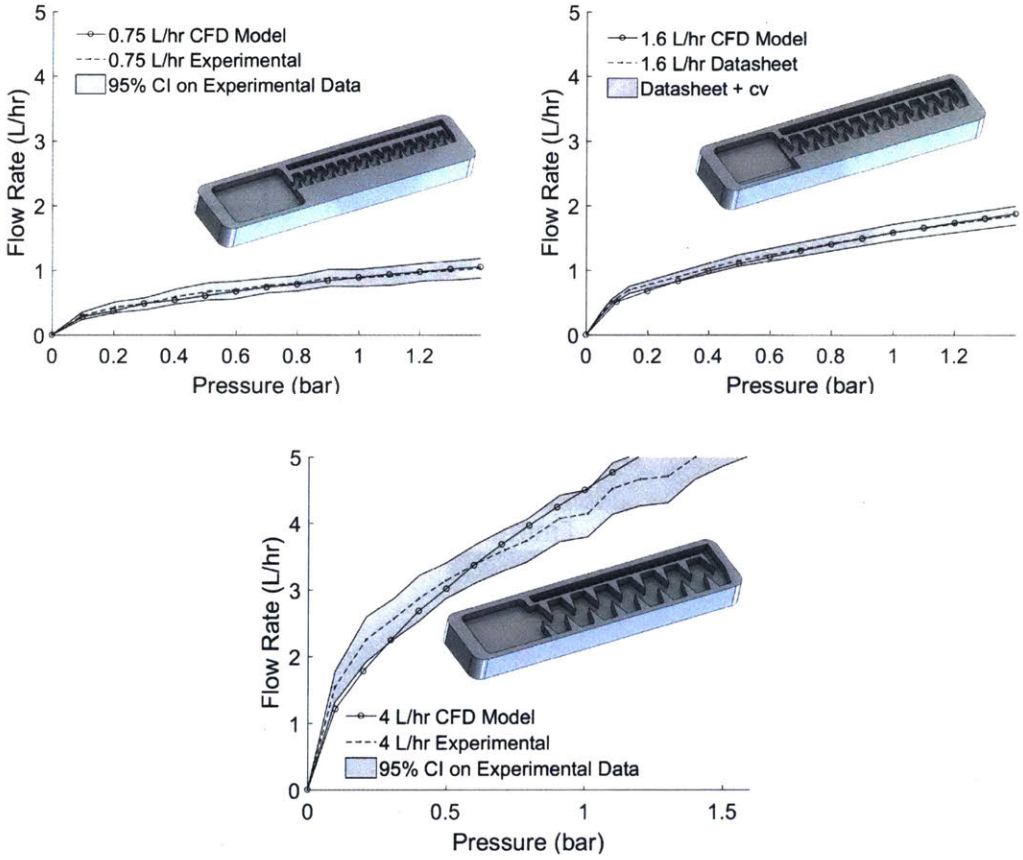

Figure 3-3: **CFD model verification**. Flow rate behavior as a function of pressure as predicted by the CFD model, datasheet values published by Jain, and experimental data collected by the authors.

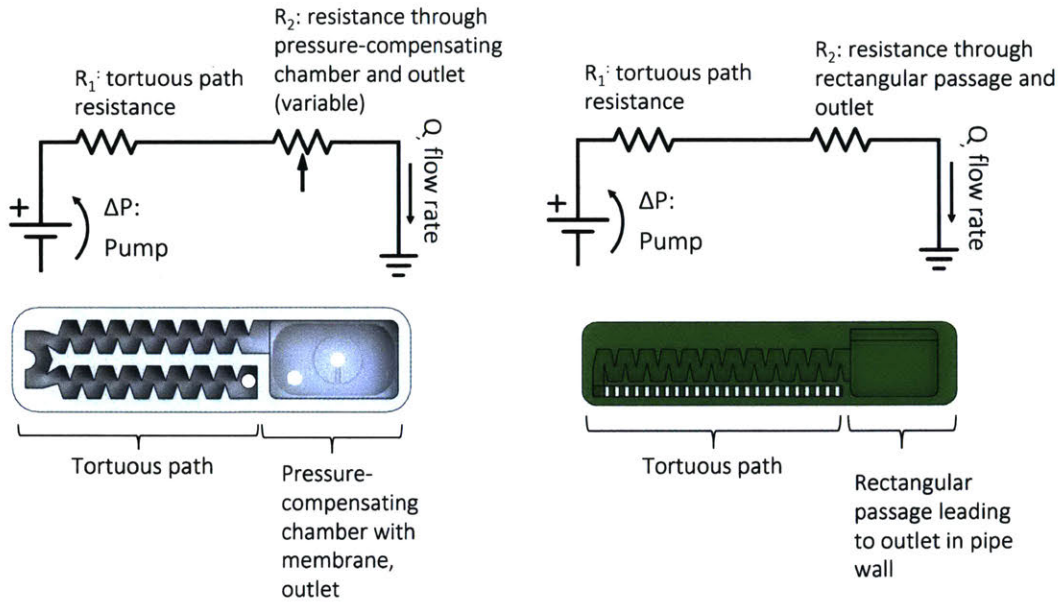

Figure 3-4: **Circuit analogy of flow resistance in PC and NPC emitters**. NPC and PC emitters have two major resistances: R_1, the resistance through the tortuous path and R_2, the resistance after the path. In PC emitters, R_2 is a variable resistance.

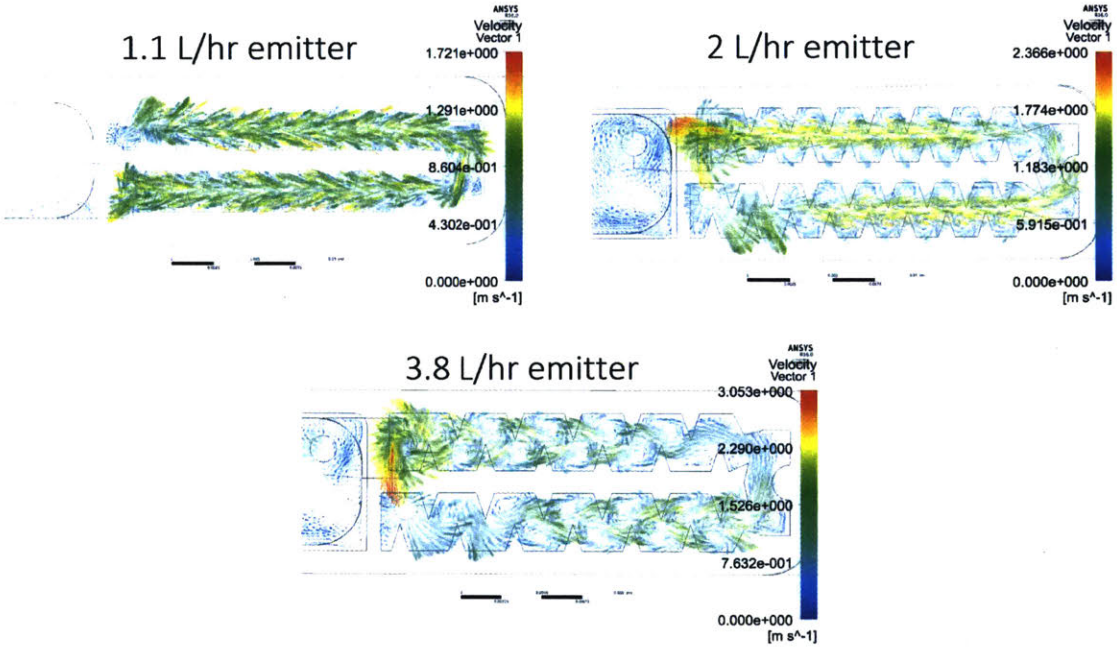

Figure 3-5: **Flow visualizations generated using ANSYS for flow through tortuous paths in Turbo Cascade 1.1, 2, and 3.8 L/hr inline drip emitters.**

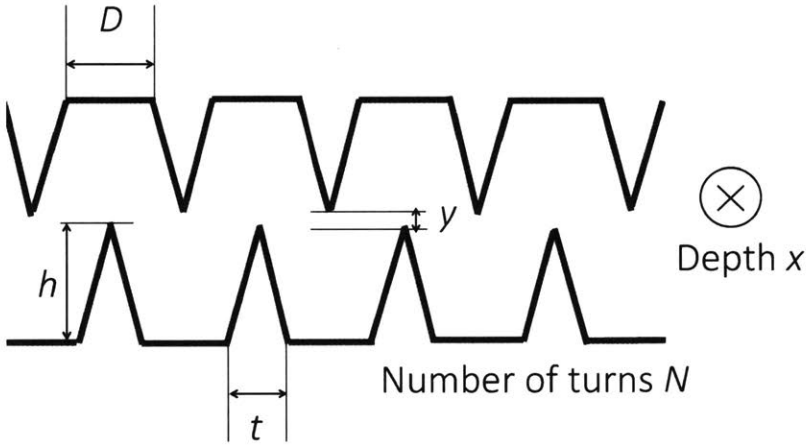

Figure 3-6: **Tortuous path geometry**. Six variables define the design of the path

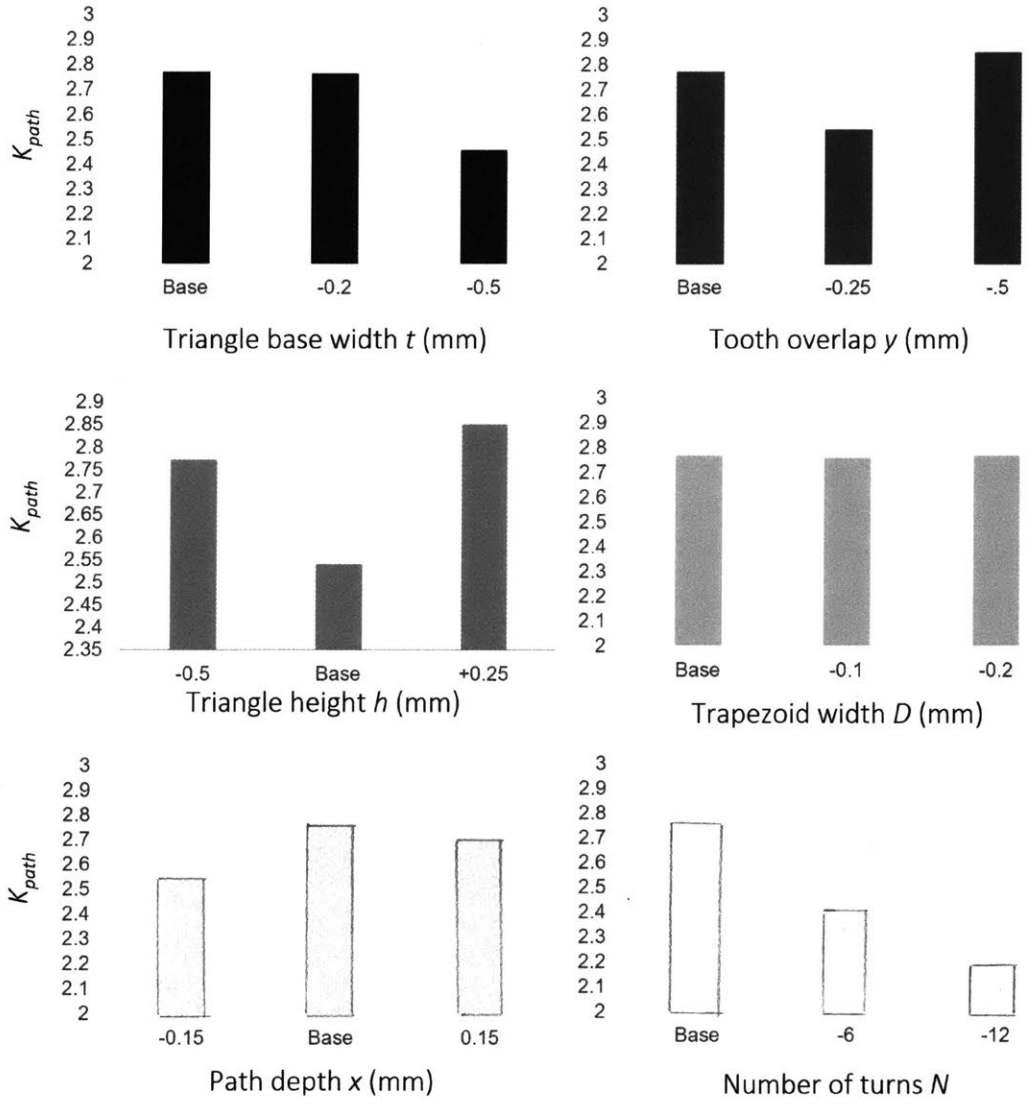

Figure 3-7: **Sensitivity of K_{path} on path geometry.**

Chapter 4

Description of pressure-compensating behavior

In a PC emitter, after the flow passes through the tortuous path, it enters into a chamber underneath a silicone membrane (Figure 1-4). To pass from the tortuous path into the chamber, the flow must undergo two 90 degree turns as it moves through a small chamber between the emitter and the pipe. The minor losses associated with these turns are accounted for in the flow modeling section.

The water enters the chamber underneath the emitter at a pressure P_2 that is much lower than the input pressure P_1 of the flow entering the emitter above the membrane. The outlet (Figure 1-4) is open to atmospheric pressure, P_a. The resulting pressure differentials across the membrane cause the membrane to deflect (Figure 4-1). As P_1 increases, the membrane deflects further and further into the chamber until it hits the lands at pressure P_L. For pressures greater than P_L, the flow must move through the small channel that passes through the lands to reach the emitter outlet.

After the membrane touches the lands, the lands apply a contact force on the membrane. For $P_1 > P_L$, the membrane deforms into the channel [26]. The magnitude of obstruction is a function of the input pressure P_1. At higher input pressures, the magnitude of deformation is greater, leading to a higher flow resistance in the channel. Because the flow resistance is greater for greater input pressures, the emitter pressure-compensates. For a range of pressures beginning with the activation pressure, P_a,

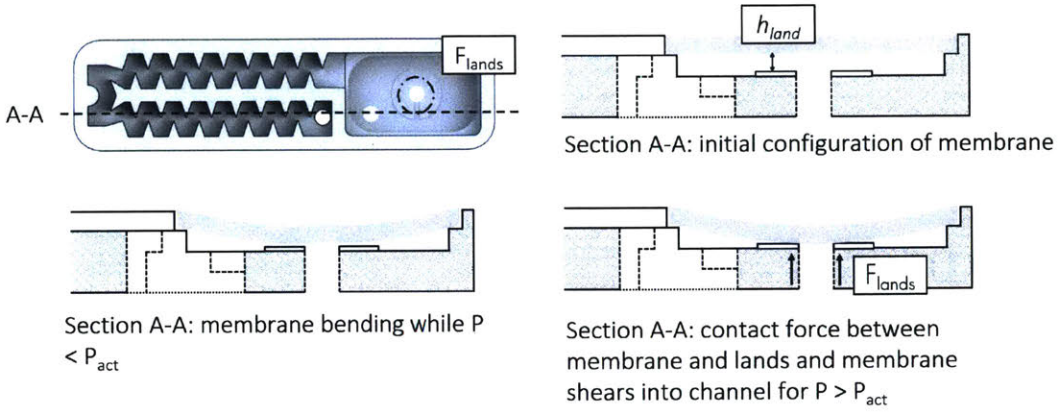

Figure 4-1: **Cross-sectional view of the pressure-compensating chamber in an inline drip emitter**

water leaves the emitter at a constant flow rate (Figure 1-3).

4.1 Membrane bending for $P_1 < P_L$

Before the membrane touches the lands, the loading on the membrane can be modeled as the linear superposition of a uniform load and a patch load (Figure 4-2). The membrane was modeled as a rectangular plate with four simply supported edges. The dimensions of the membrane were taken as the distances between each set of parallel supports. The membrane is the same size in the 1.1, 2, and 3.8 L/hr Turbo Cascade emitters and has length a of 7.0 mm, width b of 12.0 mm, and thickness h of 1.15 mm. The membrane is made of silicone rubber and has a Young's modulus E of $0.8 * 10^6$ Pa, a shear modulus G of $6 * 10^5$ Pa, and a Poisson's ratio ν of 0.48.

The uniform load is due to the loading $P_1 - P_2$ across the surface of the membrane. The patch load is due to the additional loading $P_2 - P_a$ over the emitter outlet where the membrane is exposed to atmospheric pressure (Figure 1-4).

The deflection of the membrane due to the uniform load, $w_{uniform}$, can be modeled using a Navier double series solution [32],

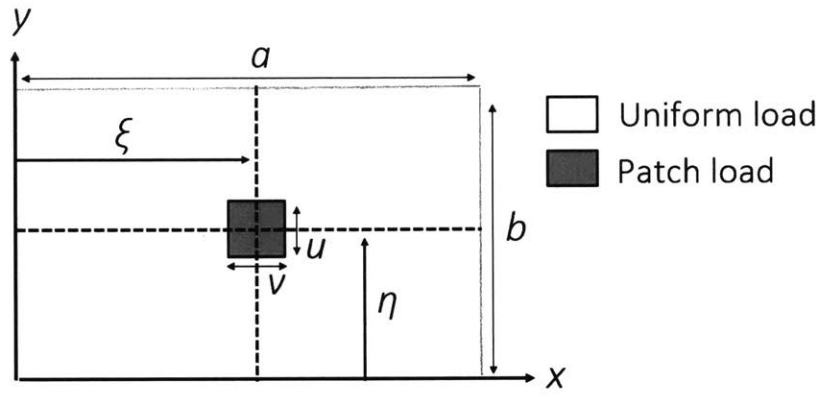

Figure 4-2: **Loading on membrane for** $P_1 < P_L$. Before the membrane touches the lands, the loading on the membrane can be modeled as the superposition of a uniform load and a patch load.

$$w_{uniform}(x,y) = \frac{16(P_1 - P_2)}{D\pi^6}\left(\frac{\sin\frac{\pi x}{a}\sin\frac{\pi y}{b}}{(\frac{1}{a^2}+\frac{1}{b^2})^2} + \frac{\sin\frac{3\pi x}{a}\sin\frac{\pi y}{b}}{3(\frac{9}{a^2}+\frac{1}{b^2})^2} + \frac{\sin\frac{\pi x}{a}\sin\frac{3\pi y}{b}}{3(\frac{1}{a^2}+\frac{9}{b^2})^2} + \frac{\sin\frac{3\pi x}{a}\sin\frac{3\pi y}{b}}{9(\frac{9}{a^2}+\frac{9}{b^2})^2}\right). \tag{4.1}$$

D is the flexural modulus of the membrane, and is given by Equation 4.2.

$$D = \frac{Eh^3}{12(1-\nu^2)} \tag{4.2}$$

Though the emitter outlet is circular, for symmetry the patch was approximated as a rectangular patch of the same area as the circular outlet (Figure 4-2). The deflection of the membrane due to the patch load, w_{patch}, can also be modeled using a Navier double series solution [32],

$$w_{patch}(x,y) = \frac{16(P_1 - P_2)}{D\pi^6}\left(\frac{\sin\frac{\pi\eta}{a}\sin\frac{\pi\xi}{b}\sin\frac{\pi u}{2a}\sin\frac{\pi b}{2b}\sin\frac{\pi x}{a}\sin\frac{\pi y}{b}}{(\frac{1}{a^2}+\frac{1}{b^2})^2}\right.$$
$$+\frac{\sin\frac{3\pi\eta}{a}\sin\frac{\pi\xi}{b}\sin\frac{3\pi u}{2a}\sin\frac{\pi b}{2b}\sin\frac{3\pi x}{a}\sin\frac{\pi y}{b}}{3(\frac{9}{a^2}+\frac{1}{b^2})^2}+\frac{\sin\frac{\pi\eta}{a}\sin\frac{3\pi\xi}{b}\sin\frac{\pi u}{2a}\sin\frac{3\pi b}{2b}\sin\frac{\pi x}{a}\sin\frac{3\pi y}{b}}{3(\frac{1}{a^2}+\frac{9}{b^2})^2}$$
$$\left.+\frac{\sin\frac{3\pi\eta}{a}\sin\frac{3\pi\xi}{b}\sin\frac{3\pi u}{2a}\sin\frac{3\pi b}{2b}\sin\frac{3\pi x}{a}\sin\frac{3\pi y}{b}}{9(\frac{9}{a^2}+\frac{9}{b^2})^2}\right), \quad (4.3)$$

where η, ξ, u, and v are defined in Figure 4-2.

The Navier double series solutions assume linear behavior. Material tests were conducted by the research team on silicone rubber using ASTM D412 [33] as a guideline. Figure 4-3 shows the results of the tests, and the range of dimensionless loading relevant to drip emitters. While the material shows strain softening for large loadings, the behavior of the membrane in the range of interest is linear, justifying the use of the Navier double series solutions to model the bending of the membrane in the emitter. Because the models are linear, they can be superimposed. The total deflection of the membrane, w_{bend}, before touching the lands is given by

$$w_{bend} = w_{uniform} + w_{patch}. \quad (4.4)$$

4.2 Membrane bending for $P_1 > P_L$

For $P_1 > P_L$, the membrane is in contact with the lands (Figure 4-2). The lands exert a contact force on the membrane, constraining the deflection along the lands. The contact force can be approximated as a partial circular line load applied at the inner land diameter. The deflection profile imposed by a circular line load on a rectangular membrane is asymmetric. To the author's knowledge, no expressions exist in literature suitable for modeling the circular lands force as a line load on the rectangular membrane.

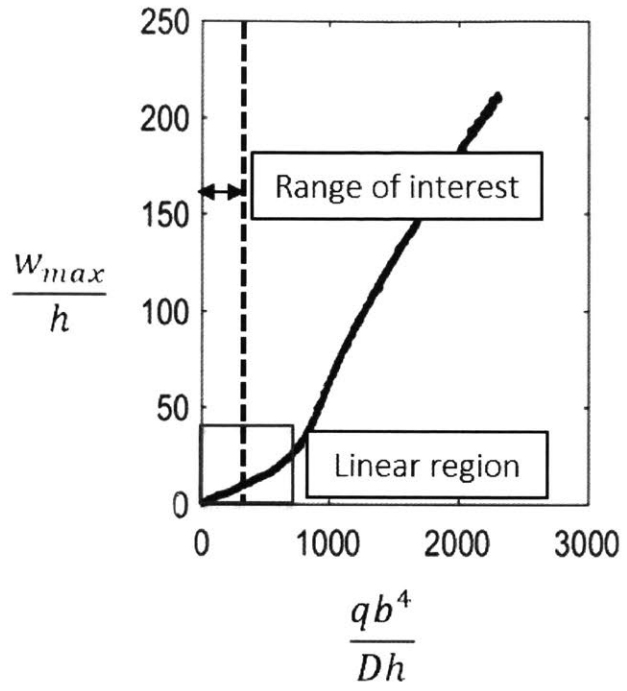

Figure 4-3: **Experimental results for a rubber tensile test**. Dimensionless deflection as a function of dimensionless loading for silicone rubber, where q is the loading applied during the test, w_{max} is the measured maximum deflection, b is membrane length, D is the flexural modulus of the membrane, and h is the membrane thickness.

The line load along the lands was approximated as a series of concentrated loads (Figure 11). The deflection of a rectangular membrane, w_{conc}, due to a concentrated load F_{lands} at (n, m) is given by the expression

$$w_{conc}(x,y) = \frac{4F_{lands}}{Dab\pi^4}\left(\frac{\sin\frac{\pi n}{a}\sin\frac{\pi m}{b}}{(\frac{1}{a^2}+\frac{1}{b^2})^2}\sin\frac{\pi x}{a}\sin\frac{\pi y}{b} + \frac{\sin\frac{3\pi n}{a}\sin\frac{\pi m}{b}}{3(\frac{9}{a^2}+\frac{1}{b^2})^2}\sin\frac{3\pi x}{a}\sin\frac{\pi y}{b}\right.$$
$$\left. + \frac{\sin\frac{\pi n}{a}\sin\frac{3\pi m}{b}}{3(\frac{1}{a^2}+\frac{9}{b^2})^2}\sin\frac{\pi x}{a}\sin\frac{3\pi y}{b} + \frac{\sin\frac{3\pi n}{a}\sin\frac{3\pi m}{b}}{9(\frac{9}{a^2}+\frac{9}{b^2})^2}\sin\frac{3\pi x}{a}\sin\frac{3\pi y}{b}\right). \quad (4.5)$$

The deflection at each coordinate (x, y) along the lands is known based on the geometry of the emitter. For $P_1 > P_L$, the deflection along the lands must equal the distance between the surface supporting the membrane and the top surface of the lands, h_{land} (Figure 4-1). The value of F_{lands} at each point along the lands can be

solved for using the compatibility condition

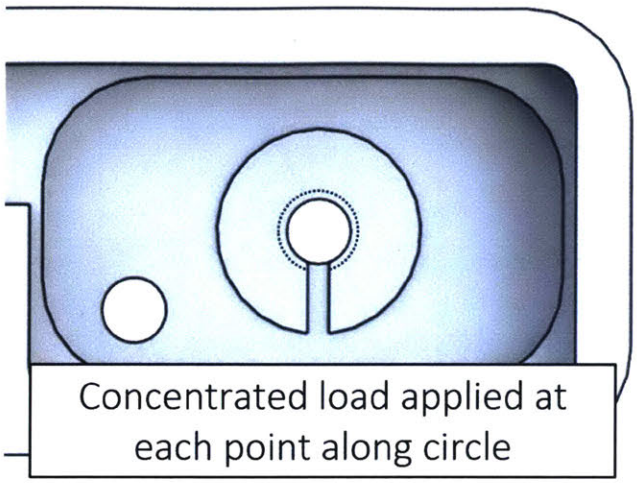

Figure 4-4: **Contact force between membrane and lands**. The contact force between the membrane and lands can be modeled as a series of concentrated forces. Each dot in the dotted line represents a location at which a concentrated force was applied.

$$\Sigma w_{conc}(x_{lands}, y_{lands}) + w_{bend}(x_{lands}, y_{lands}) = h_{land}. \tag{4.6}$$

A series of concentrated loads was applied along the lands. No loads were applied along the width of the channel (Figure 4-4). The number of concentrated loads applied along the lands was increased until the behavior of the membrane converged at seventy-two loads.

A derivative-free optimization method was used to find the set of F_{lands} that best satisfied the compatibility condition. Given an initial guess for the vector F_{lands}, the deflection at each point (x, y) along the lands due to the uniform load, patch load, and each concentrated load was calculated. The error at each point (x, y) was taken as the difference between the calculated deflection and h_{land}. The objective function was defined as the sum of the errors at each point (x, y) along the circle. The optimization found the set of F_{lands} that minimized the objective function. The optimization was

completed for each applied $P_1 > P_L$.

Figure 4-5 illustrates the deflection of the membrane due to w_{bend}, Σw_{conc}, and the total bending due to w_{bend} and Σw_{conc}. Tracing the combined loading curve confirmed that the compatibility condition along the lands was satisfied. The addition of the contact force along the lands changed the shape of the deflection profile. Inside the inner diameter of the lands, the membrane curved upwards slightly.

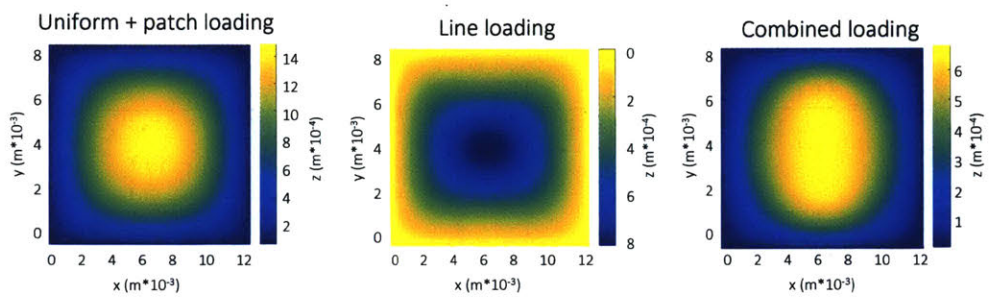

Figure 4-5: **Bending deflection visualization immediately after the membrane touches the lands in a 2 L/hr inline drip emitter**

4.3 Membrane obstruction into channel for $P_1 > P_L$

After the membrane contacts the lands, it begins to deflect into the channel. The total deflection of the membrane is the greatest at the center of the membrane near the outlet of the emitter. As the applied pressure increases, the membrane deforms into more of the channel. The deformation of the membrane into the channel effectively increases the length of the channel through which the flow must pass. As the input pressure increases, the cross-sectional area of the channel also decreases. This is the primary source of the increasing flow resistance that causes pressure-compensating behavior.

A recent study on online PC emitters [26] used thick beam theory to model the shearing behavior of a section of the membrane into the channel. The thick beam model for a clamped beam was used in the hybrid model as a basis, in order to approximate the cross-sectional profile of the membrane across the channel width.

Finite element analysis was used to scale the profile to accurately model the magnitude of the obstruction.

The length of the beam was the width of the channel, w_{ch}; the width of the beam was the length of the channel l_{ch}; and the thickness of the beam was the thickness of the membrane h. From hyperbolic shear deformation theory, the deflection, w_{beam}, of a clamped thick beam due to bending and shearing is given by [34]

$$w_{beam}(x,y) = \frac{(P_1 - P_L)w_{ch}^4}{2Eh^3}\left(\frac{x^4}{w_{ch}^4} - 2\frac{x^3}{w_{ch}^3} + \frac{x^2}{w_{ch}^2}\right) + \frac{3}{5}\frac{(P_1 - P_L)w_{ch}^2}{Gh}\left(\frac{x}{w_{ch}} - \frac{x^2}{w_{ch}^2} - \frac{\cosh\frac{\lambda w_{ch}}{2} - \cosh\lambda\left(\frac{L}{2} - x\right)}{\cosh\frac{\lambda w_{ch}}{2}}\right). \quad (4.7)$$

The constant λ is given by the expressions

$$\lambda^2 = \frac{12GC_0}{Eh^2A_0}/\left(\frac{B_0}{A_0} - A_0\right), \quad (4.8)$$

$$\lambda^2 = \cosh\frac{1}{2} - 12\left(\cosh\frac{1}{2} - 2\sinh\frac{1}{2}\right), \quad (4.9)$$

$$B_0 = \cosh^2\left(\frac{1}{2}\right) + 6(\sinh(1) - 1) - 24\cosh\frac{1}{1}\left(\cosh\frac{1}{2} - 2\sinh\frac{1}{2}\right), \textit{and} \quad (4.10)$$

$$B_0 = \cosh^2\left(\frac{1}{2}\right) + \frac{1}{2}(\sinh(1) + 1) - 4\cosh\frac{1}{2}\sinh\frac{1}{2}. \quad (4.11)$$

The study by Shamshery and Winter [26] linearly superimposed the predicted bending and shearing deformations for the thick beam with the bending deformation of the membrane. In this study, the thick beam model only was used to provide a linear basis upon which to apply correction functions derived from finite element analysis. The thick beam model assumes that the span/depth and span/width ratios of the beam structure are significantly large to justify modeling the structure as a beam. Models for beams of relatively great depth and width become considerably less accurate for span/depth ratios less than 3 [35]. The section of the membrane that shears into the channel has a span/depth ratio of 0.5, which is considerably less than the lower bound of the recommended range for beam modeling.

Finite element simulations can be used to provide more accurate estimates on how the membrane deforms into the channel. A finite element model of a membrane shearing into a channel was built using ANSYS Mechanical 16.0. The membrane was modeled as a neo-Hookean solid. The model used a rectangular mesh of shell elements and defined a frictional contact with Gauss point detection between the membrane and lands structure. Figure 4-6 shows the maximum deflection of the membrane as a function of pressure, as compared to the thick beam model.

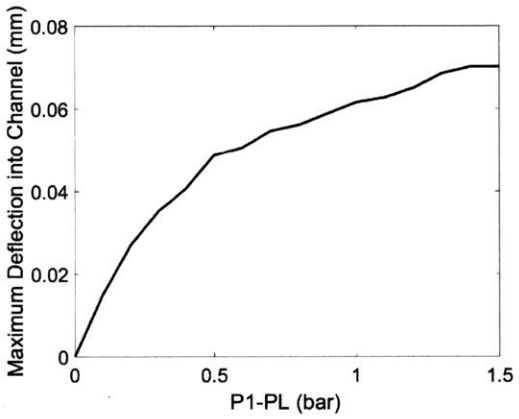

Figure 4-6: **The maximum deflection along the channel increases nonlinearly with pressure**

To incorporate the information from the finite element simulation into the hybrid model, the results from FEA were used to define correction functions to apply to the linear predictions of the thick beam model (Figure 4-7). Figure 4-8 shows the correction functions used for the 2 L/hr emitter. The finite element model was used to find the percentage of the channel into which the membrane was deformed and the average deflection of the membrane over only that portion of the channel, for a wide range of pressures (Figure 4-8). The scale factor was defined as the ratio between the average deflection of the portion of membrane obstructing the channel, as predicted using FEA, and the deflection predicted by thick beam theory (Equation 4.7).

The resulting correction functions (Figure 4-8) were used in the hybrid analytical-computational model for the geometry and flow resistance through the channel with high accuracy for $P_1 > P_L$. The thick beam model predicts a linearly increasing

deflection with pressure. The scaled deflection profile as a function of pressure was approximately parabolic, as in the finite element results (Figure 4-6).

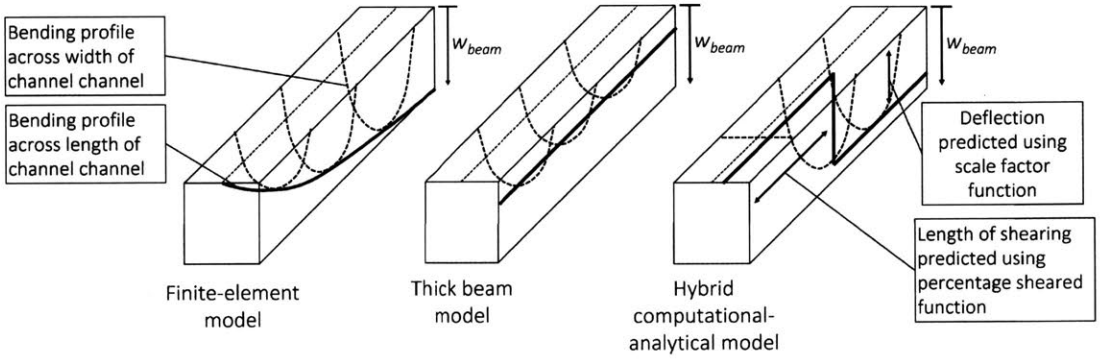

Figure 4-7: **The hybrid-analytical model incorporates results from FEA simulations using scaling relationships**

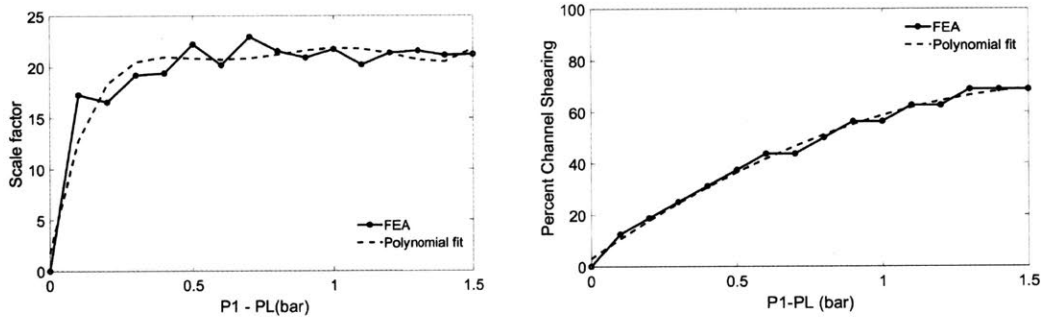

Figure 4-8: **Scaling functions describing membrane obstruction into channel**. Polynomials were fit to results from the FEA model to create expressions for a scaling factor and percent channel shearing as a function of pressure. The finite element model was used to find the percentage of the channel into which the membrane had sheared and the average deflection of the membrane over only that portion of the channel.

4.4 Flow Modeling

After the fluid passes from the tortuous path into the chamber under the membrane, the flow through the channel and out of the emitter outlet was modeled analytically. The analytical model of online emitters by Shamshery and Winter [26] used the

Darcy-Weisbach equation to model the flow under the channel. The Darcy-Weisbach equation for flow through a duct gives [36]

$$P_2 - P_a = \frac{1}{2}\rho\frac{fL}{D_h}(v_{darcy})^2 + \frac{\rho(v_{darcy})^2}{2}\Sigma K_{minorloss}. \tag{4.12}$$

In this expression f is the friction factor, L is the length of the duct, and D_h is the hydraulic diameter of the duct. $K_{minorloss}$ are the minor loss coefficients for irregularities in the duct geometry. In this model, minor losses for the flow moving out of the labyrinth, into the chamber underneath the membrane, into the channel, and through the outlet were accounted for. The magnitude of $K_{minorloss}$ depends on the diameters of the passageway before and after the change in duct dimension and can be estimated using the expression [36]

$$K_{minorloss} = (1 - \frac{D_1^2}{D_2^2})^2. \tag{4.13}$$

The variables f and D_h depend on the cross-sectional profile and area of the duct and were calculated by integrating along the duct profile, defined by the expressions for the bending and shearing of the membrane described earlier. f was calculated implicitly using the Colebrook interpolation formula [36] using an absolute roughness of 0.0015 mm, estimated from the literature for drawn plastic pipes [37], [38],

$$\frac{1}{f^{\frac{1}{2}}} = -2.0\log(\frac{\epsilon/D_h}{3.7} + \frac{2.51}{Re_{D_h}f^{\frac{1}{2}}}). \tag{4.14}$$

CFD simulations of channel-scale flow by the author shows that the Darcy-Weisbach equation for duct flow has large inaccuracies for flows of this scale. It is hypothesized that this discrepancy is due to the significance of shear stress and boundary layers in flows through the emitter. The Law of the Wall [36], which accounts for shear stresses in the flow adjacent to the wall, was applied to more accurately model the

flow. Taking v_{darcy} as the velocity in the center of the duct, the average velocity, v_{avg}, through the duct was found using the equations:

$$\frac{v_{darcy}}{v^*} = \frac{1}{\kappa}\ln(\frac{v^* D_h}{2v_f}) + B, and \tag{4.15}$$

$$\frac{v_{avg}}{v^*} \approx 2.44\ln(\frac{v^* D_h}{2v_f}) + 1.34, \tag{4.16}$$

where v^* is the friction velocity of the flow, v_f is kinematic velocity of the fluid, and κ and B are dimensionless constants with values of 0.41 and 5.0 respectively.

Chapter 5

Results and Conclusions

The methods outlined in chapters 3 and 4 were combined into a hybrid computational-analytical model that fully describes the behavior of PC inline drip emitters.

5.1 Model results

The hybrid computational-analytical model was used to predict flow rate as a function of pressure for three models (1.1, 2, and 3.8 L/hr) of the Turbo Cascade PC emitter. The inline emitter flow rates were measured (Figure 3-2) by flowing water of controlled pressure through drip tubing with 1.1, 2, and 3.8 L/hr embedded inline emitters, measuring the pressure in the pipe near the inlet of the dripper using a pressure gauge, and measuring the flow rate out of the dripline using a graduated cylinder and timer. Figure 5-1 compares the results of the CFD model to experimental results and shows the geometry of each emitter. Figure 5-1 also reports the 95 percent confidence interval for the experimental measurements, which ranged from 0.30 to 0.40 L/hr for the 3.8 L/hr emitter, from 0.21 to 0.26 for the 2 L/hr emitter, and from 0.14 to 0.24 L/hr for the 1.1 L/hr emitter.

The flow rate behavior as a function of pressure predicted by the hybrid computational-analytical model (Figure 5-1) reliably overlapped with the 95 percent confidence interval of the experimental data, validating the model predictions. Aggregated data on emitter performance published by Jain Irrigation [39] are similar to model predictions

and experimental data (Figure 5-1). Due to limitations of the experimental set-up, no data could be collected in range 0-0.32 bar with the 3.8 L/hr emitter, 0-0.3 bar with the 2 L/hr emitter, and 0-0.23 bar with the 1.1 L/hr emitter.

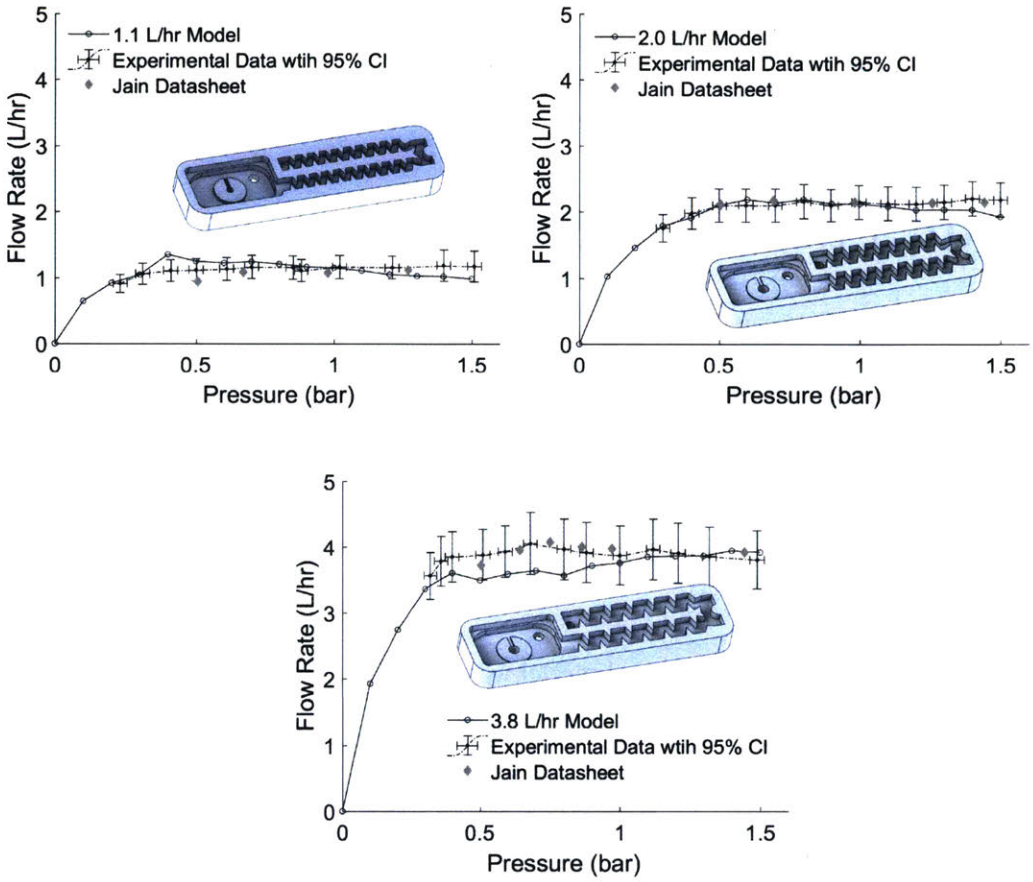

Figure 5-1: **Flow rate behavior as a function of pressure as predicted by the hybrid computational-analytical model, and experimental data collected by the author.**

5.2 Discussion

The hybrid computational-analytical model accurately predicted pressure-compensating behavior and the flow rate of three distinct emitter geometries. The model has a wider range of applicability than published analytical models, in that it accounts for flow behavior through tortuous paths, and pressure-compensating mechanisms

that include asymmetrical membrane deformation and flow channel obstruction. The hybrid model has improved accuracy when compared to the only published purely analytical model [26].

In order to incorporate the results from CFD and FEA into the model, some simplifications were made. The flow resistance after the tortuous path was approximated as constant to calculate the path scaling parameter. Additionally, an averaged representation of the obstruction of the membrane into the channel was used (Figure 5-1). The contact force between the membrane and the lands was also approximated as a series of concentrated loads; in actuality, the contact is a continuously distributed load applied on an increasing area. While the Law of the Wall improved the accuracy of the flow rate as predicted by Darcy-Weisbach, the analytical expressions are still a simplified representation of the actual flow behavior. These approximations contribute to some error in the model.

Generating the high-resolution CFD model predictions for a given path geometry presented in Figures 3-3 took four to six hours using five 2.4 GHz Intel Xeon Processor cores in parallel, dependent on the geometry of the path. Modeling the contact between the membrane and the lands, and coupling the fluid-structure interactions in a computational model would add significantly more to this time. The computational time required to fully model an emitter makes model-based design optimization extremely time and resource intensive. Using the same processor, the hybrid computational-analytical model presented herein can generate predictions of the same resolution in approximately 30 minutes and can be used to optimize and iterate designs much more efficiently than full CFD simulations.

5.3 Conclusions and future work

CFD and FEA are powerful but computationally intensive methods of modeling the behavior of inline drip emitters. The involved user input needed to change emitter geometry, and the long processing time to run simulations make it difficult to optimize the designs of drip emitters with tortuous paths and complex geometries using

only computational models. Using a hybrid computational-analytical model significantly reduces the computational time required to model and optimize the behavior of PC inline drip emitters while maintaining a high level of accuracy. The model and techniques presented in this thesis can be used with a wide range of geometries.

This method can be used to improve the design of inline drip emitters to lower the activation pressure and material costs associated with manufacturing the emitter. The tortuous path scaling parameter and dimensions of the pressure-compensating chamber could be used as variables in an optimization to minimize the emitter activation pressure, volume of material in the emitter, or otherwise improve the design of an emitter. Future work on this topic should include a range of design optimization, and a broad model to predict the analytically predict the flow behavior through a variety of path geometries.

Bibliography

[1] Irrigation Museum. Irrigation timeline. Web, 2017.

[2] S. A. Kulkarni, F. B. Reinders, F. Ligetvari, and Megh R. Goyal. *Sustainable Micro-Irrigation: Principles and Practices*, chapter Pressured Irrigation Technology: Global Scenario. Apple Academic Press, 2015.

[3] Private correspondance with jain irrigation inc, 2016. Jalgao, India.

[4] Y. Glaad. Hydraulic and mechanical properties of drippers. In *Proceedings of the Second International Drip Irrigation Conference*, Riverside, CA, 1974.

[5] United Nations Enviornment Programme. Sourcebook of alternative technologies for freshwater augmentation in some countries in Asia. Technical report, 1998.

[6] S. Phansalkhar and S. Verma. *Silver Bullets for the Poor: Off the Business Park*. IWMI-Tata Water Policy Program, 2008.

[7] International Development Enterprise. Technical manual for ideal micro-irrigation systems. Technical report, IFAD and UN Environment Programme, 2013.

[8] Energy Sector of the South Asia Regional Office. India power supply to agriculture. Technical report, Document of the World Bank, 2001.

[9] Pulkit Shamshery and Jaya Narain. Cost optimization of drip irrigation systems. Technical report, Unpublished, 2016.

[10] Roopal Suhag. Overview of ground water in india. Technical report, PRS Legislative Research, 2016.

[11] Department of Agriculture and Cooperation. Indian agricultural census. Web, 2010-2011.

[12] N. S. L. Srivastava. Farm power sources, their availability and future requirements to sustain agricultural production. Technical report, Indian Council of Agricultural Research.

[13] United States Agency for International Development. Improving water security and climate resilience in morocco. (Web), 2016. accessed Feb. 2017.

[14] David Bainbridge. Buried clay pot irrigation, June 2001.

[15] International Commission on Irrigation and Drainage. Drip irrigation. Web, 2012.

[16] Irrigation Direct. Drip irrigation history and benefits. Web, Sept 2011.

[17] Sandra Postel. Drip irrigation expanding worldwide. In *âĂć*. National Geographic, 2012. Web.

[18] Food and Agricultural Organization. Pressured irrigation techniques: Low-cost family drip irrigation techniques. Web, 2007.

[19] International Development Enterprises. An entryway into high value produce markets. Web, 2016.

[20] DFID Knowledge and Research Programme. Low cost micro irrigation technologies for the poor. Web, October 2003.

[21] Shilp Verma, Stanzin Tsephal, and Tony Jose. Pepsee systems: grassroots innovatoins under groundwater stress. *Water Policy*, November 2003.

[22] Soloman Jeeya, Roytre Laloo, and Bhanu Mishra. Traditional agricultural practices in meghalaya, north east india. *Indian Journal of Traditional Knowledge*, January 2006.

[23] G. Palau-Salvador, J. Aryiza-Valverde, and V.F. Bralts. Hydraulic flow behavior through an in-line emitter labyrinth using cfd techniques. In *ASAE*, St. Joseph, MO, 1974.

[24] Y. Dazhuang, Y. Peiling, R. Shumei, L. Yunkai, and X. Tingwu. Numerical study on flow property in dentate path of drip emitters. *New Zealand Journal of Agricultural Research*, pages 705–712, 2007.

[25] Q. Wei, Y. Shi, W. Dong, G. Lu, and S. Huang. Study on hydraulic performance of drip emitter by computational fluid dynamics. *Agricultural Water Management*, 84:130–136.

[26] P. Shamshery, R. Wang, D. Tran, and A.G. Winter V. Modeling the future of irrigation: a parametric description of pressure compensating drip irrigation emitter performance. *PlosOne*, 2017.

[27] W. Zhengying. The step-by-step cfd design method of pressure-compensating emitter. *Engineering Sciences*, 11:62–67, 2013.

[28] W. Wang, V. Bralts, and J. Wang. A hydraulic analysis of an online pressure compensating emitter using cfd-csd technology. In *ASAE Annual International Meeting*, Dallas, TX, 2012.

[29] Jain Irrigation Systems Ltd. Jain turbo excel. Web, 2016.

[30] Irrigation Training and Research Center. Low-pressure testing: Micro-irrigation emitters. Technical report, 2013. Report No. R 13-004.

[31] L. Yongxin, L. Guangyong, Q. Xiangyu, W. Jiandong, and M. Alam. Computational fluid dynamics analysis and verification of hydraulic performance in drip irrigation emitters. In *Irrigation Association International Irrigation Technical Conference*, Phoenix, AZ, 2005.

[32] E. Ventsel and T. Krauthammer. *Thin Plates and Shells: Theory, Analysis, and Applications*, chapter Rectangular Plates, pages 55–104. Marcel Dekker Inc, New York, 2001.

[33] ASTM International. Designation d412-15a: Standard test methods for vulcanized rubber and thermoplastic elastomers - tension. Web, 2016.

[34] Y. M. Ghugal and R. Sharma. A refined shear deformation theory for flexure of thick beams. *Latin American Journal of Solids and Structures*, pages 183–195, 2011.

[35] W.C. Young and R. G. Budynas. *Roark's Formulas for Stress and Strain*, chapter Beams: Flexure of Straight Bars, pages 125–188. McGraw-Hill, 2002.

[36] Frank White. *Fluid Mechanics*, chapter Viscous Flow in Ducts, pages 325–405. McGraw-Hill, 1998.

[37] J. McGovern. Technical note: Friction factor diagrams for pipe flow. Technical report, Dublin Institute of Technology, 2011.

[38] Pipeflow: fluid thinking software solutions, 2012.

[39] Jain Irrigation Systems Ltd. Jain turbo cascade pc, pcnl, and pcas. Web, 2016.